HOKKAIDO UNIVERSITY

Title	The inclined conductive column effect: a new simple model for magnetotelluric anomalous phases
Author(s)	Inoue, Tomohiro; Hashimoto, Takeshi
Citation	Geophysical Journal International, 238(3), 1825-1839 https://doi.org/10.1093/gji/ggae252
Issue Date	2024-09
Doc URL	https://hdl.handle.net/2115/92980
Rights	This article has been accepted for publication in Geophysical Journal International ©: 2024 The Authors. Published by Oxford University Press on behalf of the Royal Astronomical Society. All rights reserved.
Type	journal article
File Information	Geophysical Journal International_238.pdf

Hokkaido University Collection of Scholarly and Academic Papers : HUSCAP

Geophysical Journal International

Geophys. J. Int. (2024) **238,** 1825–1839
Advance Access publication 2024 July 22
GJI Geomagnetism and Electromagnetism

https://doi.org/10.1093/gji/ggae252

The inclined conductive column effect: a new simple model for magnetotelluric anomalous phases

Tomohiro Inoue [1,2] and Takeshi Hashimoto [3]

[1] *Graduate School of Science, Hokkaido University, N10W8, Kita-ku, Sapporo, Hokkaido* 060-0810, *Japan. E-mail: tinoue@sevo.kyushu-u.ac.jp*
[2] *Institute of Seismology and Volcanology, Faculty of Science, Kyushu University,* 744, *Motooka, Nishi-ku, Fukuoka-shi, Fukuoka* 819-0385, *Japan*
[3] *Institute of Seismology and Volcanology, Faculty of Science, Hokkaido University, N10W8, Kita-ku, Sapporo, Hokkaido* 060-0810, *Japan*

Accepted 2024 July 15. Received 2024 June 27; in original form 2023 October 8

SUMMARY

Magnetotelluric data are sometimes accompanied by 'anomalous' impedance phases (ϕ_{xy} and ϕ_{yx}) in the off-diagonal components deviating from the first ($0^\circ < \phi_{xy} < 90^\circ$) or third ($-180^\circ < \phi_{yx} < -90^\circ$) quadrant, especially in long-period bands. This phenomenon is called the phases out-of-quadrant (POQ). The POQ poses a challenge in magnetotelluric modelling because simple 1-D or 2-D models cannot explain it. Previous studies have reported that strong inhomogeneity, anisotropy, or particular 3-D structures, such as the L-shaped or cross-shaped conductors, could explain the POQ. Aside from these models, we have discovered that a slanted columnar conductor also generates the POQ. Our systematic investigation through the synthetic forward modelling of an inclined conductive column with a varying geometry showed that the inclination angle and the column length may affect the POQ appearance. We investigated herein the behaviour of the electric currents around the inclined conductive column embedded in a resistive half-space. We found that the induced electric field in the region with the POQ tends to point in the opposite direction to the surrounding vectors. This result can reasonably explain the inverted phase in long-period bands. Furthermore, we confirmed that current is sucked into one end of the column, but discharged from the other end, suggesting that the column works as a current channel. The localized reverse vectors are associated with the current channelling along the inclined conductor, which generates the POQ. A volcanic conduit within a resistive host rock is one of the typical field examples of such an inclined channel. Our study suggests that the POQ is a helpful clue in imaging the geometry of a volcanic magma plumbing system through magnetotelluric surveys.

Key words: Electromagnetic structure; Magnetotellurics; Numerical modelling.

1. INTRODUCTION

The phases of the off-diagonal components in magnetotelluric (MT) impedance tensors are usually in the first or third quadrant ($0^\circ < \phi_{xy} < 90^\circ$ and $-180^\circ < \phi_{yx} < -90^\circ$). However, anomalous phase responses that significantly deviate from this range are sometimes observed (e.g. Jones *et al.* 1988; Heise & Pous 2003; Thiel *et al.* 2009; Pavan Kumar & Manglik 2012; Ichihara *et al.* 2019; Zhang *et al.* 2021; Raju *et al.* 2022) and are called the phases out-of-quadrant (hereafter POQ). The POQ often appears only in long-period bands. 1-D or simple 2-D resistivity models cannot explain the POQ (Livelybrooks *et al.* 1996; Ichihara & Mogi 2009). In the past, the MT data with the POQ were often not used for 1-D or 2-D modelling (Heise & Pous 2003; Rippe *et al.* 2013). Therefore, the phenomenon has remained a challenge in MT modelling.

Previously proposed POQ models commonly involve a complex subsurface structure. In fact, the POQ is often encountered in MT surveys targeting volcanoes or subducting plate boundaries, where such complexity is often associated (e.g. Pous *et al.* 2002; Aizawa *et al.* 2014, 2022; Bologna *et al.* 2017; Cordell *et al.* 2019; Li *et al.* 2022). With the widespread use of 3-D MT inversion codes (e.g. Siripunvaraporn & Egbert 2009; Kelbert *et al.* 2014; Usui 2015), the POQ has also been reproduced in 3-D resistivity modelling with real field data in recent years. For example, Aizawa *et al.* (2014) revealed the existence of a large low resistivity anomaly beneath the Kirishima volcano through 3-D inversion modelling and concluded that conductors with a large resistivity contrast to the surroundings were necessary in reproducing the POQ. Likewise, other field examples also required large-scale conductive anomalies associated with a background high resistivity in reproducing the POQ (Ichihara *et al.* 2014; Aizawa *et al.* 2022).

© The Author(s) 2024. Published by Oxford University Press on behalf of The Royal Astronomical Society. This is an Open Access article distributed under the terms of the Creative Commons Attribution License (https://creativecommons.org/licenses/by/4.0/), which permits unrestricted reuse, distribution, and reproduction in any medium, provided the original work is properly cited.

Downloaded from https://academic.oup.com/gji/article/238/3/1825/7718123 by Hokkaido University user on 26 August 2024

Although the 3-D inversion analysis of some field examples has made it possible to reproduce the POQ, a physical understanding of the generation mechanism of the POQ has not yet been fully achieved. Clarifying the POQ generation conditions will contribute to facilitating model choice in MT studies. There are a few such studies as follows. Pek & Verner (1997) incorporated anisotropy in a 2-D model, demonstrating that the telluric current may be deflected and reversed on the anisotropic blocks. Furthermore, Heise & Pous (2003) investigated the conditions necessary for generating the POQ in a 2-D model and succeeded in explaining the field data accompanied by the POQ. Their study showed that for the POQ to appear, the anisotropic block must be widely distributed at a shallow depth. Weckmann *et al.* (2003), working with the real field data, explained the localized POQ adjacent to the graphitized marble ring with a shallow conductive square tube causing strong 3-D effects, while the POQ observed over a wider area was explained by anisotropy. The negative phase in the TE mode can also be explained by a 2-D structure with a strong resistivity contrast (Selway *et al.* 2012). More recently, 3-D models were proposed to explain the POQ using a good conductor with a 3-D geometry (e.g. Lezaeta & Haak 2003; Ichihara & Mogi 2009; Raju & Patro 2023). Ichihara & Mogi (2009) examined the conditions under which the POQ is generated by forward calculations using synthetic models. They found that a local convexed conductor, when combined with a regional-scale conductive anomaly caused by sea and sediments, produces the POQ in the off-diagonal components in the vicinity of the convex (i.e. L-shaped model). Raju & Patro (2023) proposed a cross-shape 3-D conductor model in a geological context to explain the POQ that appeared in the real data. Conversely, Piña-Varas & Dentith (2018) found that the POQ may appear in the off-diagonal components when a strong resistivity contrast (e.g. 2/10 000 Ω·m) is considered, even without a particular 3-D structure like an L-shaped conductor. In their model, the POQ can appear in a wide area in contrast to the L-shaped conductor model, in which it is localized around the conductive convex. Thus, although several previous studies successfully modelled the occurrence of the POQ, other models may also generate it, highlighting the need for further research.

This study proposes the inclined conductive column (ICC) effect as a simple and realistic 3-D conductivity model that the POQ can accompany. As is discussed in detail in the later sections, the ICC effect locally concentrates the electric current at the tip of a tilted conductor in a resistive host rock. This locally distorted current generates the POQ. We investigate herein how the geometry of the conductive column affects the POQ generation through systematic forward calculations.

2. THE INCLINED CONDUCTIVE COLUMN MODEL

2.1 Background and configuration of the model

The background of the idea behind the ICC effect comprises studies on the 3-D MT inversion modelling of volcanoes (e.g. Aizawa *et al.* 2022; Inoue *et al.* 2022). These studies imaged a conductive column tilting down in a specific direction from the volcanic centre and pointed out the conductors that are essential in explaining the POQ in the off-diagonal long-period component of the observed MT impedance. These studies gave us an idea that quite a simple structure (i.e. tilted conductive column) may be responsible for the generation of the POQ.

In this study, we used synthetic models to systematically examine the relationship between the POQ and the geometry of a conductive column. The model space was set up in a Cartesian coordinate with X positive northward (±294 km), Y positive eastward (±294 km) and Z positive upward ($-562 < Z < 0$ km). The central part of the model space was divided into 1 km (X) × 1 km (Y) × 1 km (Z) cells. The outer region was coarsened by a factor of two in cell size, such that the largest cell was 256 km per side. The total number of cells was 94 (X) × 94 (Y) × 58 (Z) = 512 488. Every single cell was uniform and isotropic. At the shallow centre of this model, a tilted column of resistivity ρ_1 was embedded in an otherwise uniform host medium of resistivity ρ_0. In the case of Model-I, the host medium of resistivity ρ_0 was 1000 Ω·m. The tilted angle (θ) and the depth range (Δd) of the conductive column were defined as shown in Fig. 1.

We performed forward calculations using the ModEM code (Egbert & Kelbert 2012; Kelbert *et al.* 2014) to obtain the MT impedance at 13 periods (0.01, 0.05, 0.1, 0.5, 1, 5, 10, 50, 100, 500, 1000, 5000 and 10 000 s). Figs 2–7 depict the distribution of phases on the ground surface as colour maps, with the induced electric field direction superimposed by arrows. We calculated the induced electric field from the impedance tensor in the same way as in the works of Uyeshima *et al.* (2001) and Ichihara *et al.* (2013). Let us consider the following input magnetic field variation:

$$\begin{pmatrix} B_x \\ B_y \end{pmatrix} = \begin{pmatrix} \cos(\varphi)\, e^{i\alpha} \\ \sin(\varphi)\, e^{i\alpha} \end{pmatrix}, \tag{1}$$

where φ is the azimuth angle taken clockwise positive from geographic north, and $\alpha = \omega t$ is the phase of the magnetic field. ω represents the angular frequency, and t is time. The induced electric field is presented as follows using an impedance tensor:

$$\begin{pmatrix} E_x \\ E_y \end{pmatrix} = \begin{pmatrix} Z_{xx} & Z_{xy} \\ Z_{yx} & Z_{yy} \end{pmatrix} \begin{pmatrix} \cos(\varphi)\, \mathrm{e}^{\mathrm{i}\alpha} \\ \sin(\varphi)\, \mathrm{e}^{\mathrm{i}\alpha} \end{pmatrix}. \tag{2}$$

We denote the impedance tensor by *Re* and *Im* for the real and imaginary parts, respectively.

$$\begin{pmatrix} E_x \\ E_y \end{pmatrix} = \begin{pmatrix} Re(Z_{xx}) + Im(Z_{xx})\, i & Re(Z_{xy}) + Im(Z_{xy})\, i \\ Re(Z_{yx}) + Im(Z_{yx})\, i & Re(Z_{yy}) + Im(Z_{yy})\, i \end{pmatrix} \begin{pmatrix} \cos(\varphi)\, e^{i\alpha} \\ \sin(\varphi)\, e^{i\alpha} \end{pmatrix}, \tag{3}$$

where vector ($Re(Z_{xx})$, $Re(Z_{yx})$) represents the electric field induced by the unit sinusoidal magnetic field variation in the northward direction (i.e. $\varphi = 0$) reaching the maximum amplitude (i.e. $\alpha = 0$). Likewise, vector ($Re(Z_{xy})$, $Re(Z_{yy})$) represents the electric field induced when the unit magnetic field variation reaches the maximum amplitude in the eastward direction (i.e. $\varphi = \pi/2$ and $\alpha = 0$). Vector ($Im(Z_{xx})$, $Im(Z_{yx})$) corresponds to the induced electric field when the direction of the unit magnetic field variation changes from southward to northward, and its amplitude approaches zero (i.e. $\varphi = 0$ and $\alpha = -\pi/2$). Vector ($Im(Z_{xx})$, $Im(Z_{yy})$) is the electric field induced when the magnetic amplitude approaches zero, varying from west to east (i.e. $\varphi = \pi/2$ and $\alpha = -\pi/2$).

Figs 2–7 illustrate the impedance phase of the Z_{yx} component together with the induced electric field direction (vector: $Re(Z_{xx})$, $Re(Z_{yx})$) when the magnetic field fluctuations are directed to the north and reached their maximum amplitude. Note that the vector field is displayed using arrows, indicating the direction of the vectors alone without representing their magnitudes. In the case of the Z_{xy} component, we show the induced electric field direction (vector: $Re(Z_{xy})$, $Re(Z_{yy})$) when the magnetic field fluctuation turns to the east and reaches its maximum amplitude. When mapping the phase by colour, we added 180° to the phase of the Z_{yx} component to make the comparison of the Z_{xy} and Z_{yx} components easier.

Downloaded from https://academic.oup.com/gji/article/238/3/1825/7718123 by Hokkaido University user on 26 August 2024

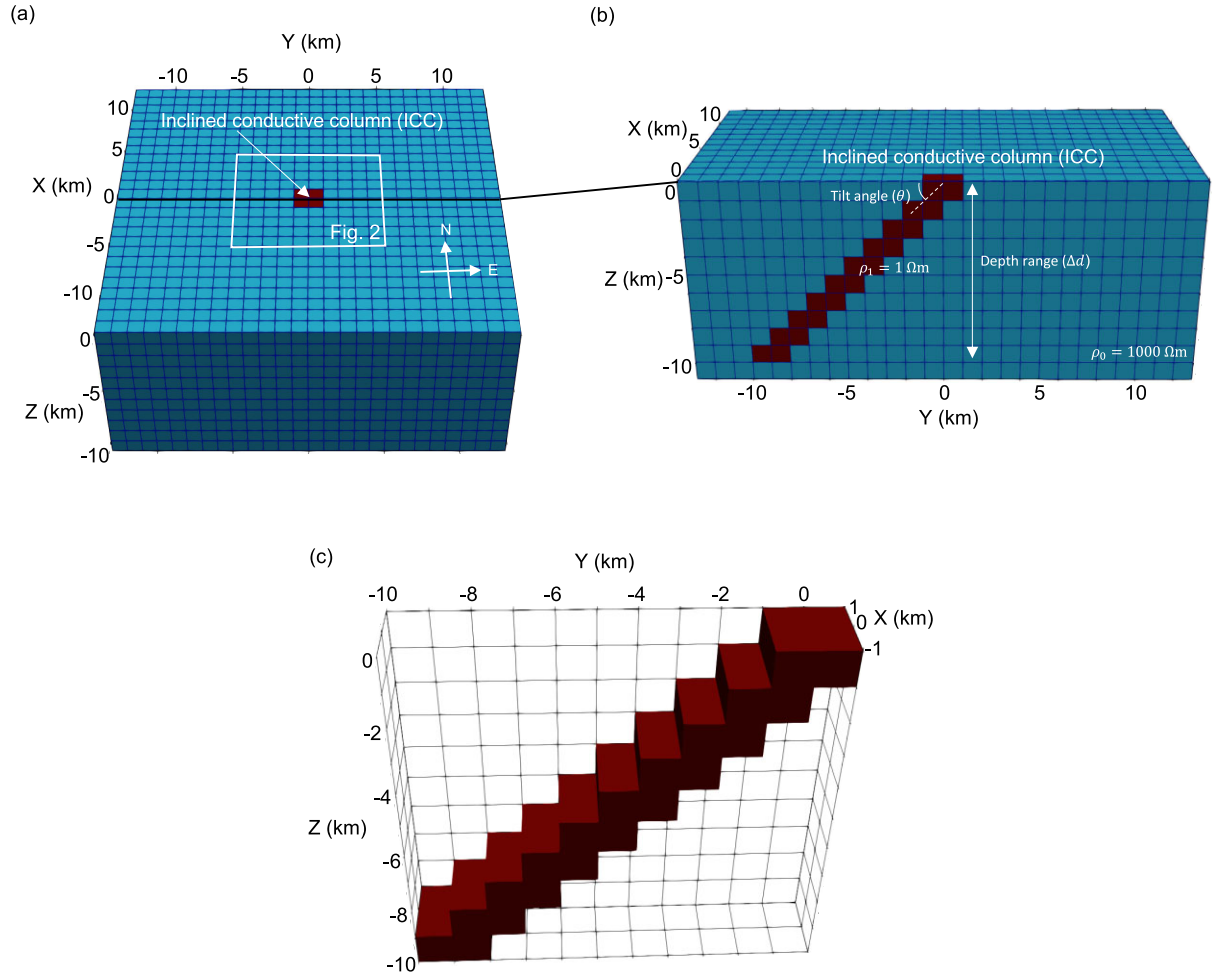


Figure 1. 3-D views of the synthetic model with an ICC (Model-I: $\theta = 45^\circ$ and $\Delta d = 10$ km). (a) Bird-eye view of the central part of the model from south. (b) Vertical section of the model at $X = 0$ km. (c) The 3-D view of the ICC extracted from Model-I.

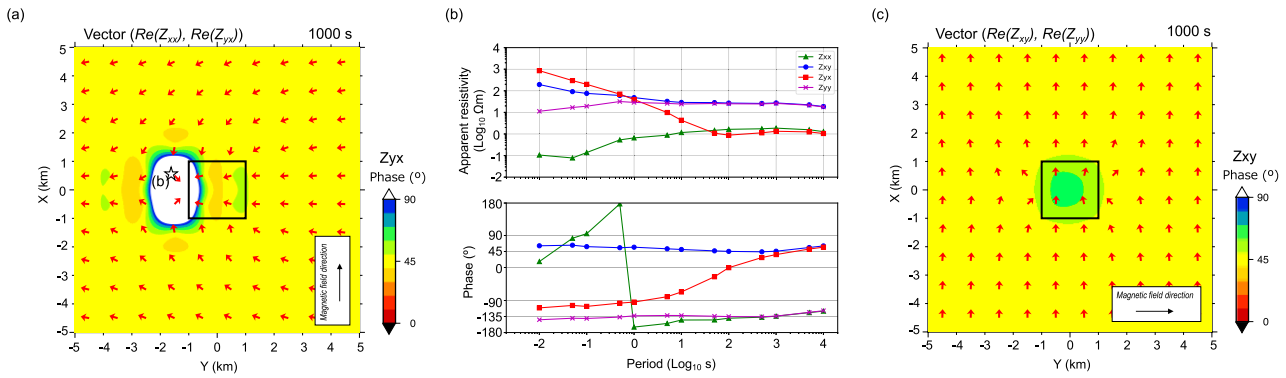


Figure 2. Response of the Model-I. (a) Phase map of the *YX* component for the area indicated by the white square in Fig. 1(a). Arrows denote the distribution of induced electric field (direction alone) due to the magnetic field variation reaching the maximum amplitude in the northward direction. The square shows the top of the ICC. (b) The sounding curves of the ICC model at the star symbol in the panel (a). (c) Phase map of *XY* component and the direction of induced E-field variation reaching maximum in the eastward direction.

2.2 Effects of tilt angle

First, we show the response of the synthetic models with a conductive column tilting westward ($\theta = 45^\circ$) and a fixed depth range $\Delta d = 10$ km, at a 1000 s period in Fig. 2 (see also Fig. 1 for the model geometry). In Fig. 2(a), the POQ of over 90° is localized on the west side of the column top shown as a black square (i.e. on the side with the column inclines). Fig. 2(b) displays the responses of the *yx* component at the test site (white star, Fig. 2a).

Downloaded from https://academic.oup.com/gji/article/238/3/1825/7718123 by Hokkaido University user on 26 August 2024

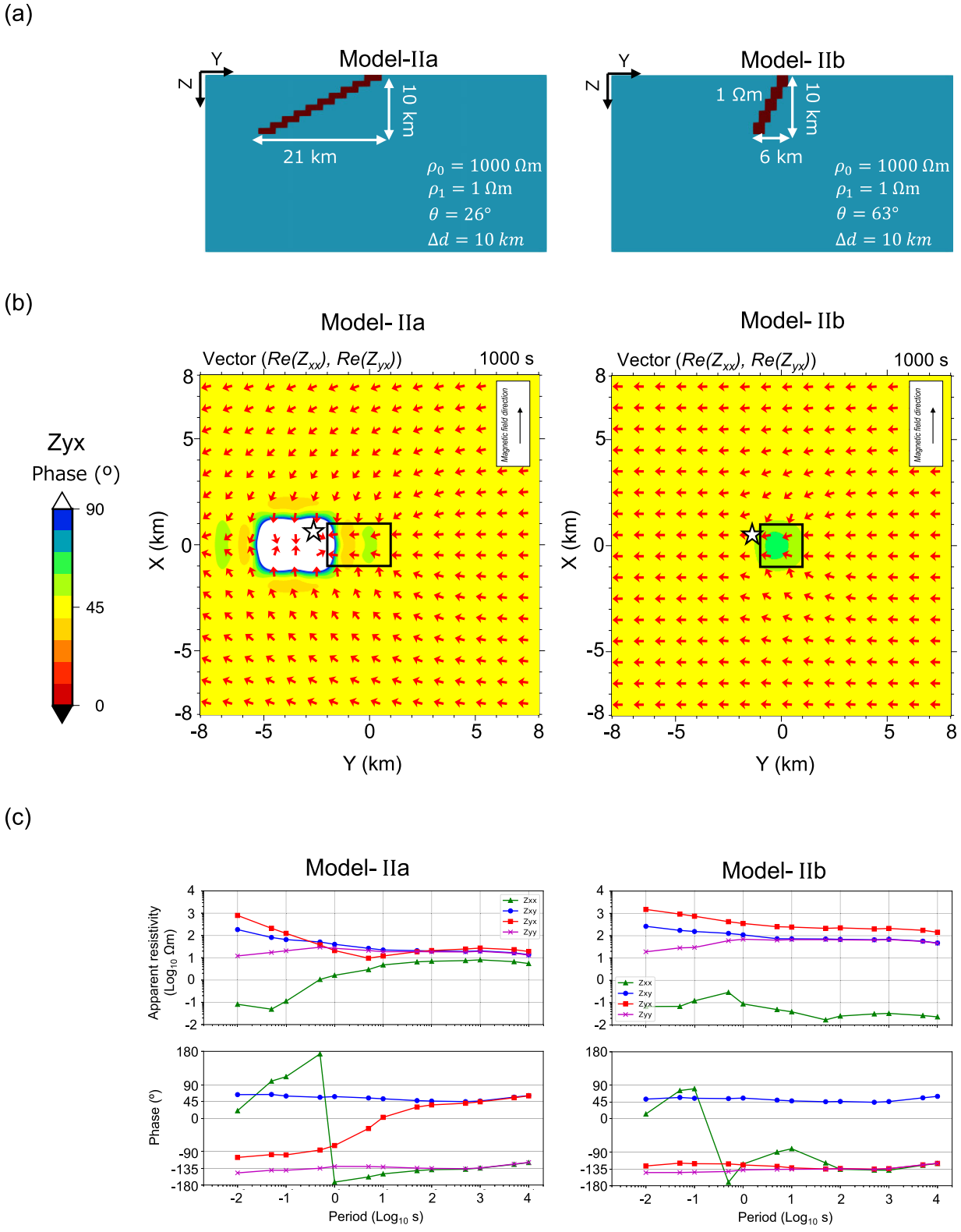


Figure 3. The responses of the models with different tilt angles of the ICC. The left-hand column shows diagrams for Model-IIa ($\theta = 26°$ and $\Delta d = 10$ km), while the right-hand column does for Model-IIb ($\theta = 63°$ and $\Delta d = 10$ km). (a) Cross-sections of the two models. (b) Phase (colour) and the E-field direction (arrows) map of the *YX* component. The square indicates the top of the ICC. (c) The sounding curves at the star symbol in (b).

Downloaded from https://academic.oup.com/gji/article/238/3/1825/7718123 by Hokkaido University user on 26 August 2024

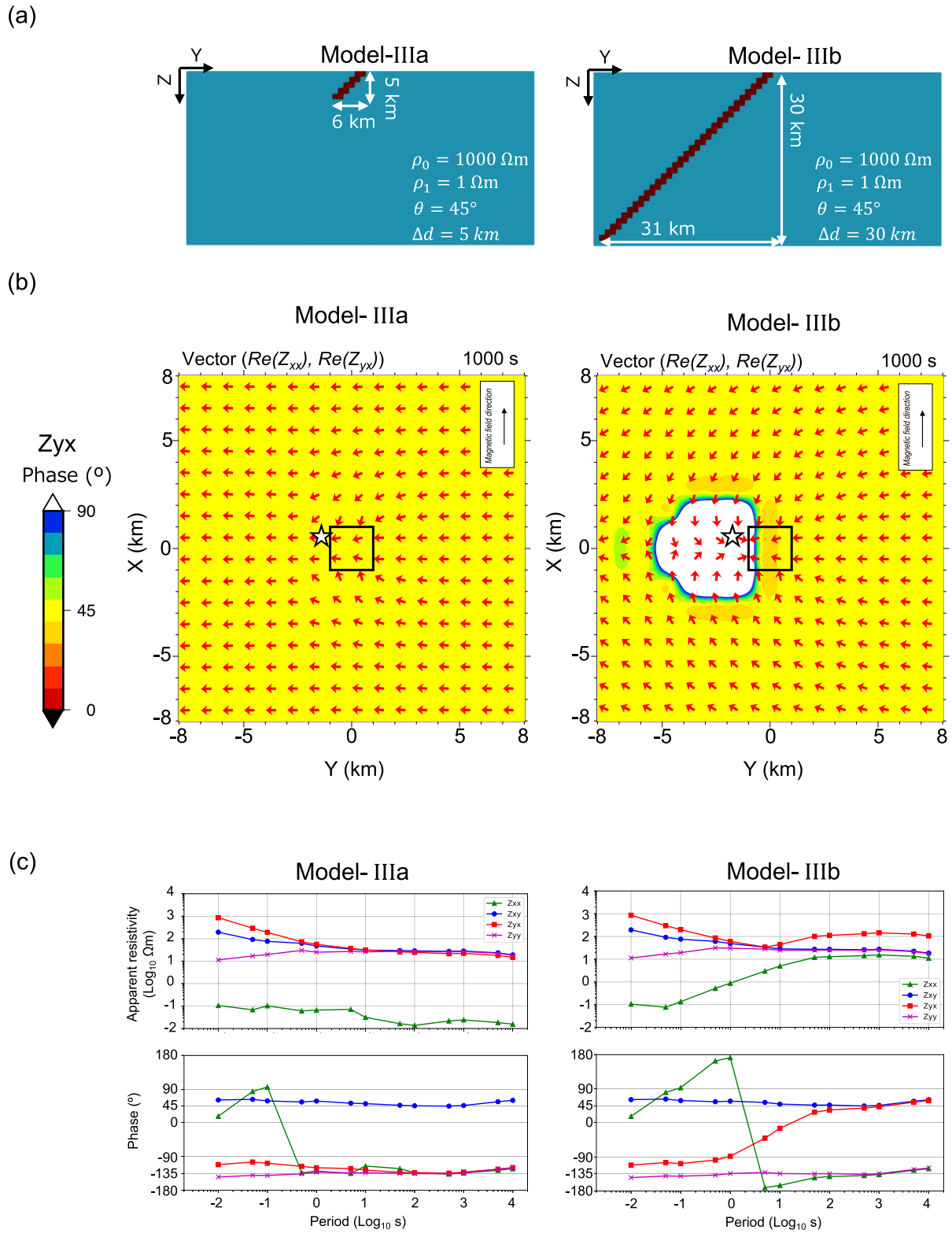


Figure 4. The responses of the Model-IIIa (left-hand column) and IIIb (right-hand column). (a) The vertical cross-sections of the models. (b) Phase (colour) and the E-field direction (arrows) map of the *YX* component. A square shows the top of the ICC. (c) The sounding curves at the star symbol in (b).

The *yx*-phase reached −90° at approximately 1 s, deviating from the normal quadrant in the period band of seconds to hours, and reaches nearly + 60° at 10 000 s (Fig. 2b). In contrast, no POQ appears in the Z_{xy} component. Next, looking at the direction of the induced electric field in Fig. 2(a), the overall electric field is induced westward when the magnetic field reaches the maximum northward. However, the

Downloaded from https://academic.oup.com/gji/article/238/3/1825/7718123 by Hokkaido University user on 26 August 2024

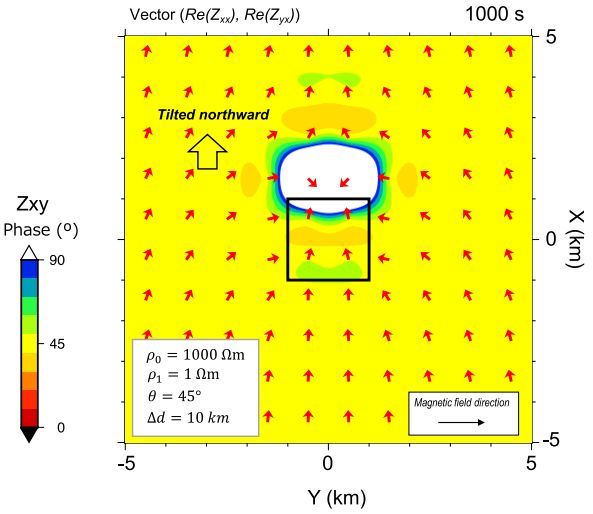


Figure 5. Phase (colours) and the E-field direction (arrows) of the *XY* component in Model-Iα in which the northward-dipping ICC is embedded. The electric field corresponds to the magnetic field approaching the maximum in the eastward direction. A square shows the top of the ICC.

induced electric field is distorted around the conductor. In particular, in the region with the POQ, the induced electric field shows a positive *Y* component in contrast to the surrounding vectors. It means an inverted phase, which is exactly what we call the POQ. This result is consistent with the fact that the phase of the Z_{yx} component at the long periods approached an almost 180° out-of-phase level with respect to the shortest period. The distribution of the electric field vectors strongly suggests that the electric field converges toward the conductive column (i.e. the telluric current is sucked into the ICC). The apparent resistivity of the Z_{yx} component indicates the resistivity of host medium ($\rho_0 = 1000$ Ω·m) at 0.01 s period and approaches to the resistivity of the ICC ($\rho_1 = 1$ Ω·m), as the period increases. Fig. 2(c) shows the phase distribution (by colour) of Z_{xy} and the direction of the induced electric field (by arrows) due to the unit magnetic field variation with a maximum amplitude in the eastward direction. In contrast to the case of Z_{yx}, no POQ appears around the conductor's top. This is also consistent with the fact that the electric field does not show a negative *X* component. We also explored Model-I using a variety of resistivity combinations other than (ρ_0, ρ_1) = (1000, 1), at periods of 10 and 1000 s, as we summarized in Fig. S1 (Supporting Information). The POQ emerges when the model had a resistivity contrast approximately over three orders of magnitudes (more exactly, over a factor of 500) across all the host rock resistivities tested here (10–1000 Ω·m) except for the case with $\rho_0 = 100$ Ω·m at a period 10 s. Furthermore, while the region where the manifested POQ remains largely unchanged (i.e. same as Fig. 2a for Model-I) with resistivity contrasts exceeding 1000, we can observe its shrinkage as the contrast approaches the lower limit of approximately 500.

Next, we examined models with different tilt angles. The left-hand side of Fig. 3 presents the model response for the tilt angle $\theta = 26°$ and the depth range $\Delta d = 10$ km (Model-IIa). In this case, the POQ can be seen in a wider area than in Model-I ($\theta = 45°$). The electric field in the POQ zone tends to show a reversed direction to the surrounding vectors, as in the case of Model-I (Fig. 2a). In the apparent resistivity plots (Fig. 3c; Model-IIa), the curves tend to significantly drop from 1000 to 10 Ω·m from the short- to long-period bands. By contrast, in the case of $\theta = 63°$ and $\Delta d = 10$ km (Model-IIb), the phase of the Z_{yx} component does not exceed 90°; thus, no POQ emerges (Fig. 3b; Model-IIb). The phase curves also denoted that both the Z_{xy} and Z_{yx} components are within the normal quadrants at all periods (Fig. 3c; Model-IIb). The apparent resistivity curve of the *yx* component indicates 1000 Ω·m, which is the host rock value at 0.01 s. However, unlike Models-I and IIa, it slowly drops toward the long-period side, falling not lower than 100 Ω·m, even at 10 000 s. Although the induced electric fields ($Re(Z_{xx})$, $Re(Z_{yx})$) are distorted to some extent around the ICC, no inverted vectors are recognized (Fig. 3b; Model-IIb).

2.3 Effects of depth range

In the next step, we examined the models with the fixed tilt angle and tilt azimuth of the conductive column and a varying depth range Δd. The left-hand column of Fig. 4 shows the response of Model-IIIa that incorporated a conductive column with a tilted angle of $\theta = 45°$, a tilt direction of $-Y$ (westward) and a depth range of $\Delta d = 5$ km. In Fig. 4(b), Model-IIIa is not accompanied by the POQ in the Z_{yx} component. However, the POQ is distinct when we increase the depth range $\Delta d = 30$ km (Model-IIIb). In this model, the electric field vectors in the region with the POQ also have $+Y$ component, similar to the POQ region that appears in Models-I and IIa. Regarding Model-IIb, the POQ prevails in a wider area than in the Model-I (Fig. 2a), suggesting that the longer the conductive column, the greater the ability to generate the POQ at the surface. The POQ does not appear when the column is too short, as in Model-IIIa. It is worth noting that the sounding curves of the phases of Models-I and IIIb slightly differ to each other. The *yx*-phase curve of Model-I was less steep than that of Model-IIIb in the middle band (approximately 1–100 s). The former exceeds −90° at approximately 5 s period, whereas the latter does at shorter period. This also implies that a longer ICC have greater ability to generate the POQ.

2.4 Effects of tilt azimuth

Finally, we examined synthetic models with a varying tilt azimuth of the conductive column. Fig. 5 shows the response of Model-Iα, whose column carries the same tilt angle ($\theta = 45°$) and depth range ($\Delta d = 10$ km) as those of Model-I, but with an altered tilt orientation [i.e. $+X$ (northward) instead of $-Y$ (westward)]. In this case, the POQ does not appear in the Z_{yx} component, but in the Z_{xy} component near the northern edge of the ICC's top. The arrows in Fig. 5 depict the direction of the electric field induced due to the increasing magnetic field in the $+Y$-direction (eastward). The induced electric field contains a southward component inside the region where the POQ appears against the surroundings. It converged toward the ICC, suggesting that current is sucked into the conductor.

Fig. 6 exhibits the impedance phase of the Z_{xy} and Z_{yx} components on the ground surface for the conductive column tilted to the northwest (N45°W) (Model-Iβ: tilt angle $\theta = 45°$ and, depth range $\Delta d = 10$ km). The POQ is seen in the Z_{xy} and Z_{yx} components on the northern and western sides of the ICC's top, respectively. They appeared at mirror-symmetry locations about the tilt axis (Figs 6b and c). However, as common in previous cases with POQs, the induced electric field on the POQ tends to swing backward against the surroundings.

We also examined the same northwestward tilting ICC model for the cases in which the direction of the magnetic field variation was rotated 45° from the previous cases. Note that this case (Model-Iγ)

Downloaded from https://academic.oup.com/gji/article/238/3/1825/7718123 by Hokkaido University user on 26 August 2024

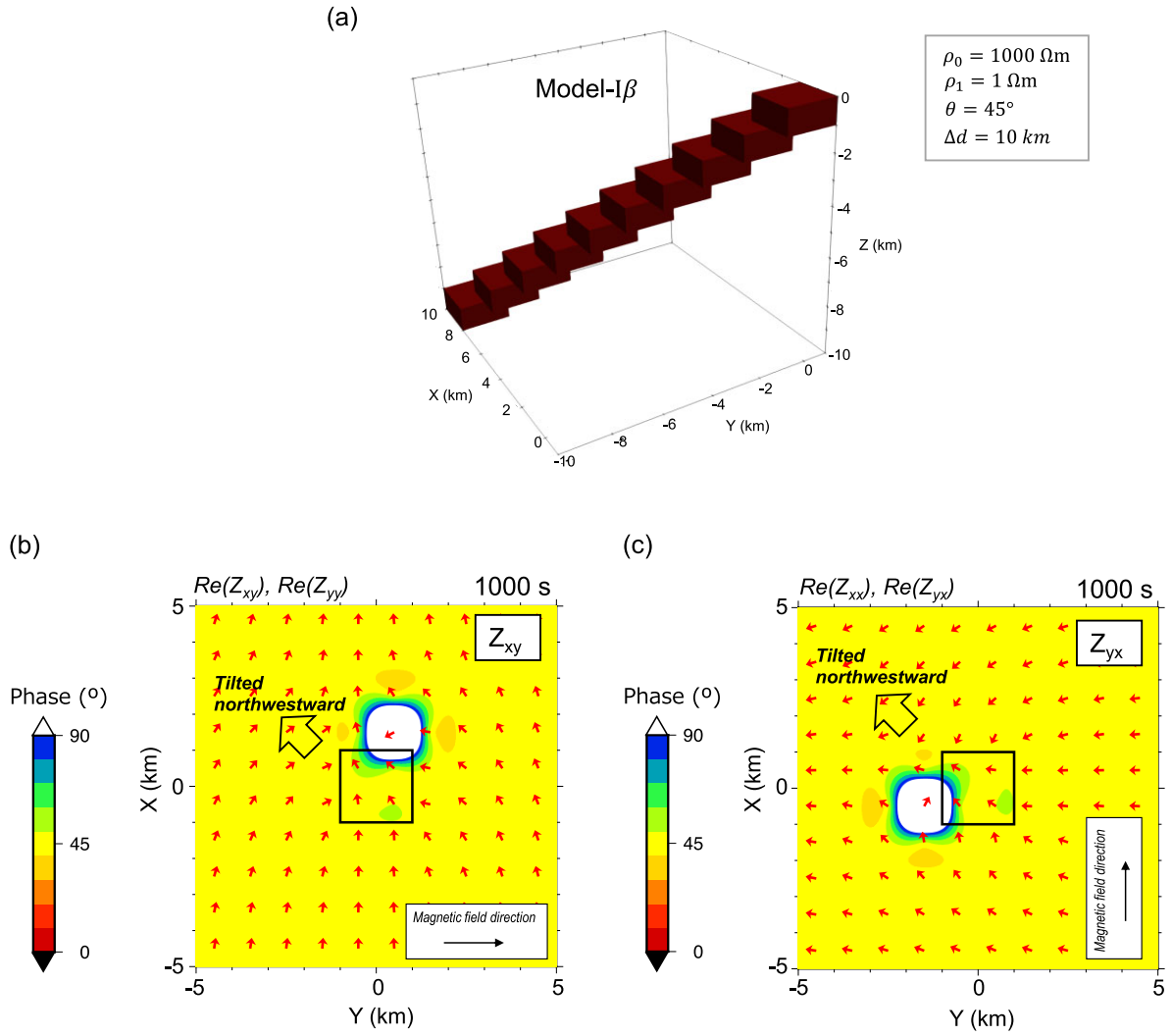


Figure 6. Responses of Model-Iβ in which the ICC dips northwestward. (a) 3-D view of the ICC in this model. (b) Phase distribution (colours) and the E-field direction (arrows) of the *XY* component, corresponding to the magnetic field approaching the maximum amplitude in the eastward direction. (c) Phase and E-field of the *YX* component, corresponding to the magnetic field approaching the maximum amplitude in the northward direction.

corresponds to the axis-rotated version of Model-I (Fig. 2). Fig. 7(a) shows the electric field induced by the magnetic field reaching the peak toward the southeast. In this case, the magnetic field is parallel to the tilt azimuth of the column, and no POQ appears in the Z_{xy} component, consistent with no induced electric field pointing southwestward. Fig. 7(b) illustrates the induced electric field corresponding to the magnetic field reaching the peak in the northeast direction. Unlike that in Fig. 6, the POQ is widely expressed in the entire northwest side of the ICC's top, in which direction the conductive column dipped (Fig. 7b). In this case, the induced electric field in the POQ region converges at the northwestern edge of the conductive column at the ground surface. Although the gridding direction of the model affects the shape of the POQ appearance, this result is essentially the same as that for Model-I (Fig. 2).

Summarizing the above-mentioned synthetic modelling results, the tilt azimuth of the ICC affects the component in which the POQ appears. However, it has less effect on the conditions for the POQ appearance due to the ICC's tilt angle, depth range and other parameters.

3. DISCUSSION

3.1 Relationship between the induced electric field and POQ

We will now investigate in detail the distribution of the induced electric field calculated from the synthetic impedance to discuss its relationship with the POQ. The left-hand column of Fig. 8 shows the response of the ICC model with $\theta = 45°$ and $\Delta d = 10$ km (Model-I) for a 1000 s period at different depth ($Z = 0$, -2, -4, -6, -8 and -10 km). The vectors indicate the induced electric field direction (horizontal component) at the moment when the northward magnetic field reaches its maximum. The colour map depicts the horizontal component intensity of the electric field. On the ground surface (i.e. $Z = 0$ km), the POQ appears on the dipping side of the ICC, and the E-field on the POQ tends to invert against the surroundings. The electric field intensity is relatively stronger on the east side of the conductive column and weaker on its top and west sides. In other words, the electric field converges toward the

Downloaded from https://academic.oup.com/gji/article/238/3/1825/7718123 by Hokkaido University user on 26 August 2024

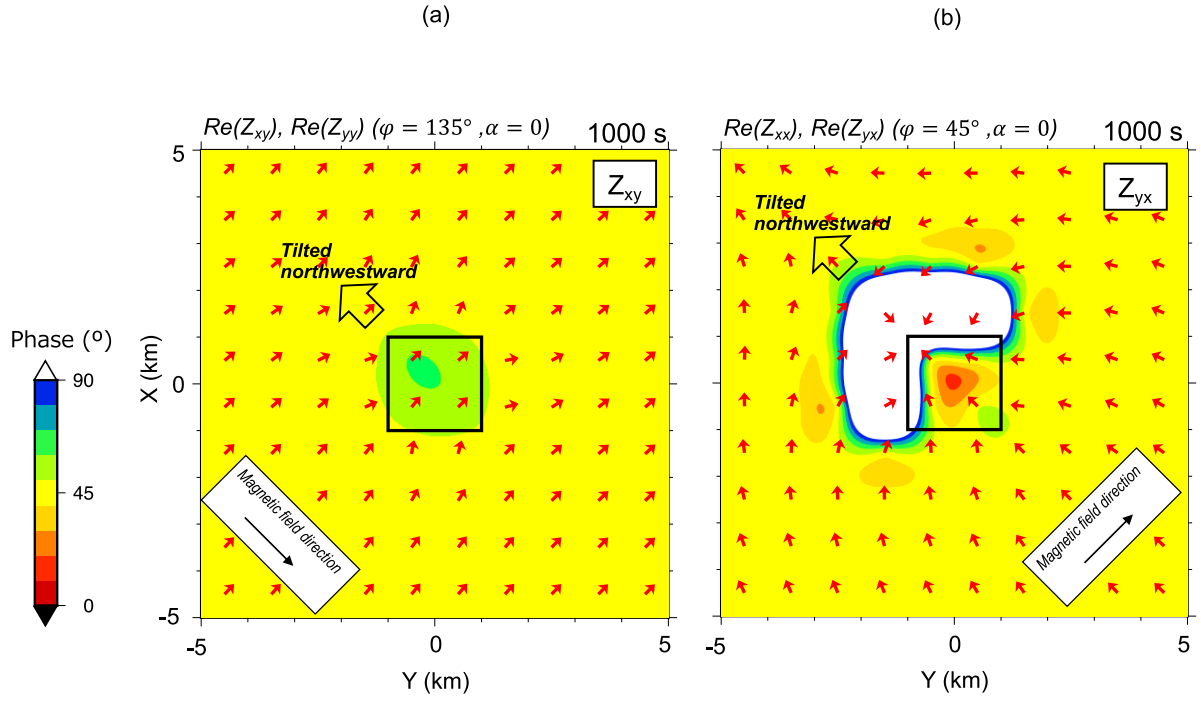


Figure 7. Responses of Model-Iγ in which the ICC dips northwestward. (a) Phase (colours) and the E-field direction (arrows) map of *XY* component, corresponding to the magnetic field variation toward the maximum amplitude in the southeast direction. (b) Phase and E-field direction map of *YX* component, corresponding to the magnetic field variation toward the maximum amplitude in the northeast direction.

ICC, and the associated electric current is sucked toward it. The electric field intensity is the weakest within the conductive column at depths of $Z = -2$ to -10 km, suggesting that the horizontally induced current is partly converted into a downward flow within the ICC. The induced electric field tends to diverge from the ICC's bottom ($Z = -10$ km). This result is also consistent with that the field intensity being relatively stronger on the west side of the ICC and weaker on its east side. The pattern looks like a mirror image of that at the ground surface. These results indicate that current is sucked at the top end of the ICC and gushed out from the bottom end. Our discussion above is based on the induction caused by the northward increasing magnetic field. Conversely, the situation is exactly reversed when the magnetic field increases southward, where the induced current is sucked in from the ICC's bottom and is spouted out at the ground surface (Fig. 9).

For a comparison with Model-I, right-hand side of Fig. 8 shows the direction and the intensity maps of the electric field induced by the northward magnetic field for Model-IIb, in which the conductive column has a geometry comprising $\theta = 63^\circ$ and $\Delta d = 10$ km and dips westward. Unlike Model-I with the POQ, a reversed electric field is found nowhere in the model space, which is consistent with the fact that Model-IIb was not accompanied by the POQ, as previously presented. The maximum electric field intensity near the ICC in Model-IIb is relatively smaller than that in Model-I. The weakest horizontal electric field is commonly seen within the conductive column, suggesting a partial conversion from horizontal to vertical current flows. Therefore, in Model-IIb, the current concentration along the ICC occurs, but the effect is not strong enough to give rise to the POQ.

We will next present the phase tensor (Caldwell *et al.* 2004), the rotational invariant Phi2 ($\Phi_2 = \sqrt{\Phi_{xx}\Phi_{yy} - \Phi_{xy}\Phi_{yx}} = \sqrt{\Phi_{max}\Phi_{min}}$), and skew ($|\beta|$) at the ground surface for Models-I and IIb. In Fig. 10(a), the phase tensor on the dipping side of the ICC indicates the high ellipticity and the extremely high skewness, suggesting that the electric field is severely distorted and that the structure is 3-D. By contrast, in Model-IIb, the phase tensor around the ICC is nearly circular and the skewness is close to zero (Fig. 10b). In short, the model has 1-D or 2-D features in terms of the impedance at the ground surface. Phi2 is close to 45° everywhere around the column top (Model-IIb), whereas it markedly exceeds 45° in Model-I in the area of the POQ appearance (i.e. western neighbour of the ICC's top). This corresponds to the fact that a conductive body (i.e. ICC) lies immediately below this region in Model-I. The absence of this feature in Mode-IIb means that a conductive column with a large dip angle does not make a significant difference in the response function from a simple vertical conductive column. In summary, the large lateral displacement between the top and bottom ends of the elongated conductive anomaly is a key condition for the structure's three-dimensionality.

Furthermore, we calculated the induction vector (Parkinson 1959; Jones 1986), which is sensitive to horizontal variations in conductivity (Fig. S2, Supporting Information). In the models with the POQ, the direction of the induction vector is such that the current is concentrated on the tilted side of the conductive column. In contrast, in the models without the POQ, the vectors simply point to the top of the conductor. However, their magnitudes are as small as 0.01 in all tested models, making them too small to be useful.

Regional induced currents may flow through narrow elongated conductors, such as a bay (Jones 1983; Arora & Adam 1992). According to Jones (1983), the current channelling by local conductors causes an anomalous phase. We consider herein that the POQ generation associated with the ICC is a phenomenon related to the induced current concentration along the ICC (i.e. current channelling). The review by Jones (1983) showed that current channelling is caused

Downloaded from https://academic.oup.com/gji/article/238/3/1825/7718123 by Hokkaido University user on 26 August 2024

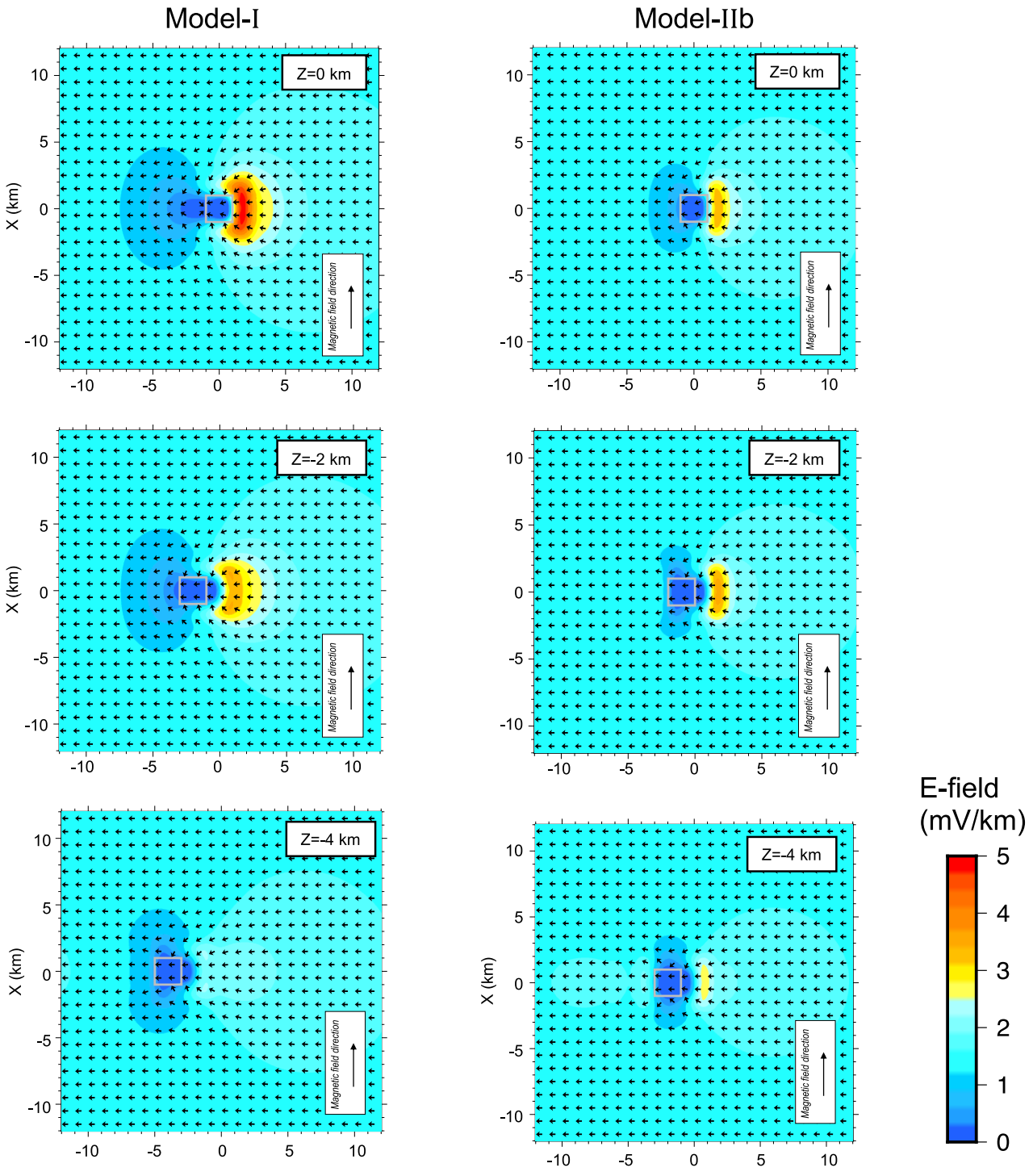


Figure 8. The induced electric field at the depth of 0, −2, −4, −6, −8 and −10 km with arrows for the direction and colours for the field intensity. The corresponding magnetic field variation is northward (1000 s period). Left-hand column shows horizontal slices of Model-I (with POQ) at various depths. Right-hand column shows those of Model-IIb (no POQ). Arrows indicate the direction of the induced electric field due to the magnetic field variation with maximum amplitude in the northward direction. The field intensity is represented with colours. The squares indicate the location of the ICC on each plane.

not by an inductive electric field, but by a quasi-static electric field created by the excess charge at the boundaries of strong resistivity contrasts, which remains even at an infinitely long period. Therefore, a strong local distortion of the electric field near the boundary between the ICC and the host rock may cause the POQ, especially for a long-period band. Specifically, in the case of Model-I, the local and quasi-static electric fields generated at the boundary between the ICC and the host rock are superposed with the regional electric field E_y, it results in the inversion of E_y, especially on the west side of the ICC, which produced the POQ in Z_{yx} component.

Downloaded from https://academic.oup.com/gji/article/238/3/1825/7718123 by Hokkaido University user on 26 August 2024

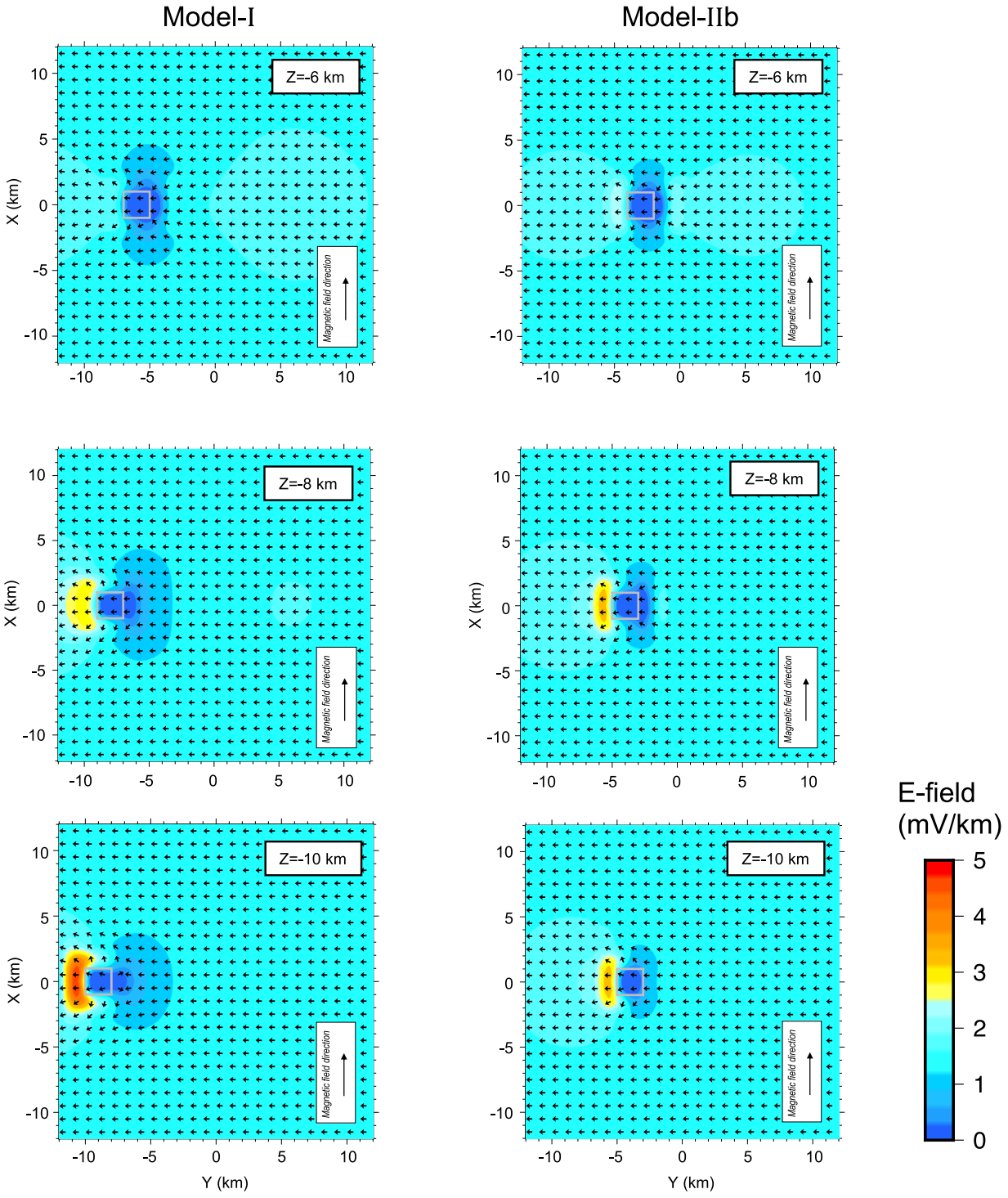


Figure 8. Continued.

In the cases examined in this study, the POQ emerges in particular component(s) and location contingent upon the ICC's geometry. Here, we consider that the POQ manifests as a result of the local reversal of the electric field direction, caused by the induction current being drawn into the ICC. Such a process efficiently arises when the ICC's azimuth aligns perpendicular to the magnetic field variations, that is, parallel to the induced electric field. In contrast, the induction current flows less readily into the conductive column when the induced electric field is perpendicular to the ICC's azimuth, resulting in no emergence of POQ. When the electric field is induced in the dipward direction of the ICC, the currents converge at its top and are channelled into the depths. Conversely, when the

Downloaded from https://academic.oup.com/gji/article/238/3/1825/7718123 by Hokkaido University user on 26 August 2024

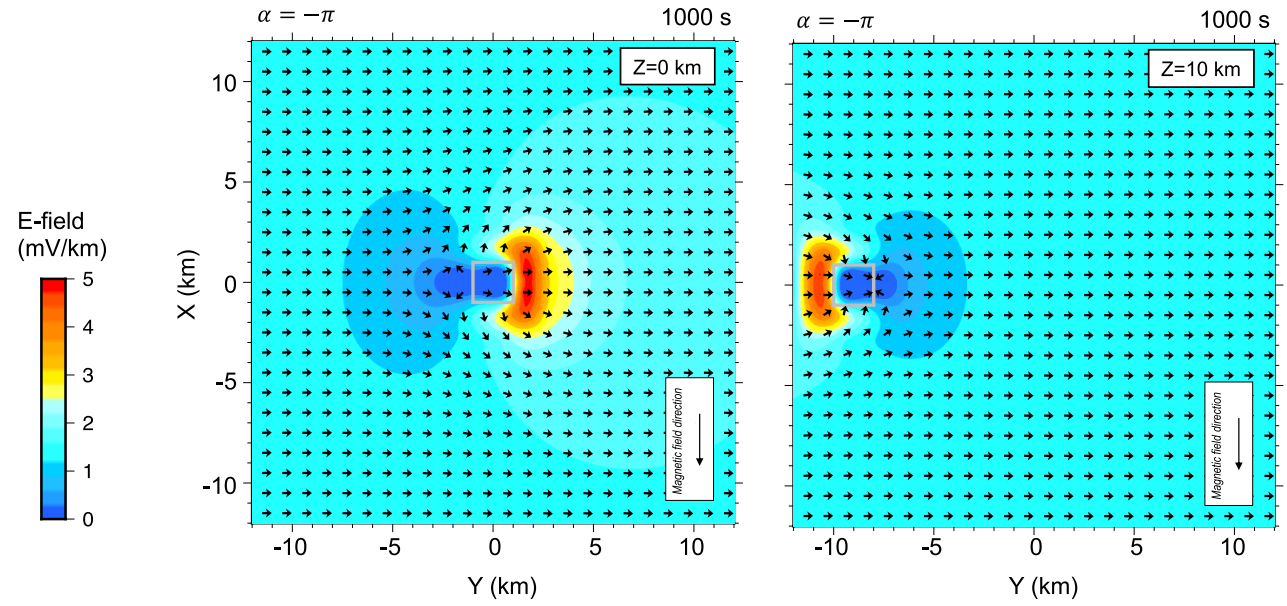


Figure 9. The induced electric field at the depth of 0 and −10 km for Model-I corresponding to the unit magnetic field variation approaching the maximum toward south. Note that the arrows indicate directions only and the field intensity is represented by colours.

electric field is induced in the opposite direction, the currents gush out and spread from the ICC's top (Fig. 11). The key point here is that in either case, the direction of the electric field can reverse with respect to the surroundings only on the dipping side of the ICC (see also Figs 2 and 5, e.g.).

3.2 Geometrical control of the ICC on the POQ generation

In Fig. 12, we summarized the result of the previous model calculations for the various combinations of the tilt angle and depth range of the conductive column to show the POQ generation conditions. The scatter plot origin (top-right corner) corresponds to the ICC's top, while the circles and the squares are plotted at the lower end position of the column for each model. The dashed line indicates the boundary of the location where the POQs were seen or not. Roughly speaking, the POQ does not occur when the lateral distance (L) between the top and bottom of the ICC is smaller than 10 km. When the conductive column dips steeply, its shape resembles a vertical pipe, making it less likely for an induced electric field in the axial direction to occur, thereby preventing current channelling. The model is accompanied by POQs when L is larger than 15 km, and the ICC extends deeper than 5 km. Meanwhile, no POQ appears in the models with a short ICC (i.e. Δd is smaller than a few km). Even under the same inclination angle, the POQ appearance depends on the ICC's depth range (Fig. 4). We interpreted that shortening the ICC made the system less responsive to long-period signals, thereby preventing channelling to occur. It is noteworthy that the POQ also disappears in a short-period band when the host medium is less resistive, despite the resistivity contrast between the host and the ICC is unchanged ($\rho_0 = 100$ Ω·m at 10 s in Fig. S1, Supporting Information). This is likely due to the reduced skin depth, resulting in a situation similar to that of a short ICC. We did not perform a further exhaustive parameter search in this work due to the model gridding and mesh spacing limitations. However, summarizing the above-mentioned results, the generation of the POQ seems strongly related to the tilt angle and length of the ICC.

The response curves may be altered depending on the ICC's geometry. For example, the apparent resistivity (ρ_{yx}) of Model-I drops to 1 Ω·m in the long-period band, while that of Model-IIa to several 10 Ω·m (Figs 2b and 3c). In Model-IIIb, ρ_{yx} shows a minimum at the period around 5 s and slightly increases toward the long-period band. We consider that such differences in responses in the long-period band across different models result from subtle variations in the direction and magnitude of electric field at the observation point, which are contingent upon the geometry of the ICC (Fig. 8 and Fig. S3, Supporting Information). Here, considering the continuity of the current, the presence of a downward current component being drawn in at the observation point would also affect the horizontal component of the electric field.

3.3 Highlights of the model and implications to field survey

The ICC model presented in this study is, to the best of our knowledge, the simplest 3-D model generating the POQ. Previous studies also proposed that particular 3-D structures generate POQs. Weckmann *et al.* (2003) modelled resistivity structures in a geological context and explained the localized POQ with a conductive ring structure (square tube) embedded in a resistive host, as well as the POQs in wider area with 2-D anisotropy. One of the important remarks based on their modelling study is that current gathering and deflection in the shallow part can cause strong 3-D effects, particularly at long periods and only in close proximity to the conductivity anomaly. Such features are partly common to our ICC model. In their modelling study, the Z_{xy} phase over 90° emerges above the square tube on the edges parallel to the x-axis and the POQ of the Z_{yx} component above the edges parallel to the y-axis. Likewise, the ICC model generates POQs in the off-diagonal component corresponding to the tilt azimuth; for example, POQ in Z_{yx} is found when the column dips in y-direction (Fig. 2). These key features of the ICC model can also be identified in their model, and in this regard, we do not consider our model to be entirely

Downloaded from https://academic.oup.com/gji/article/238/3/1825/7718123 by Hokkaido University user on 26 August 2024

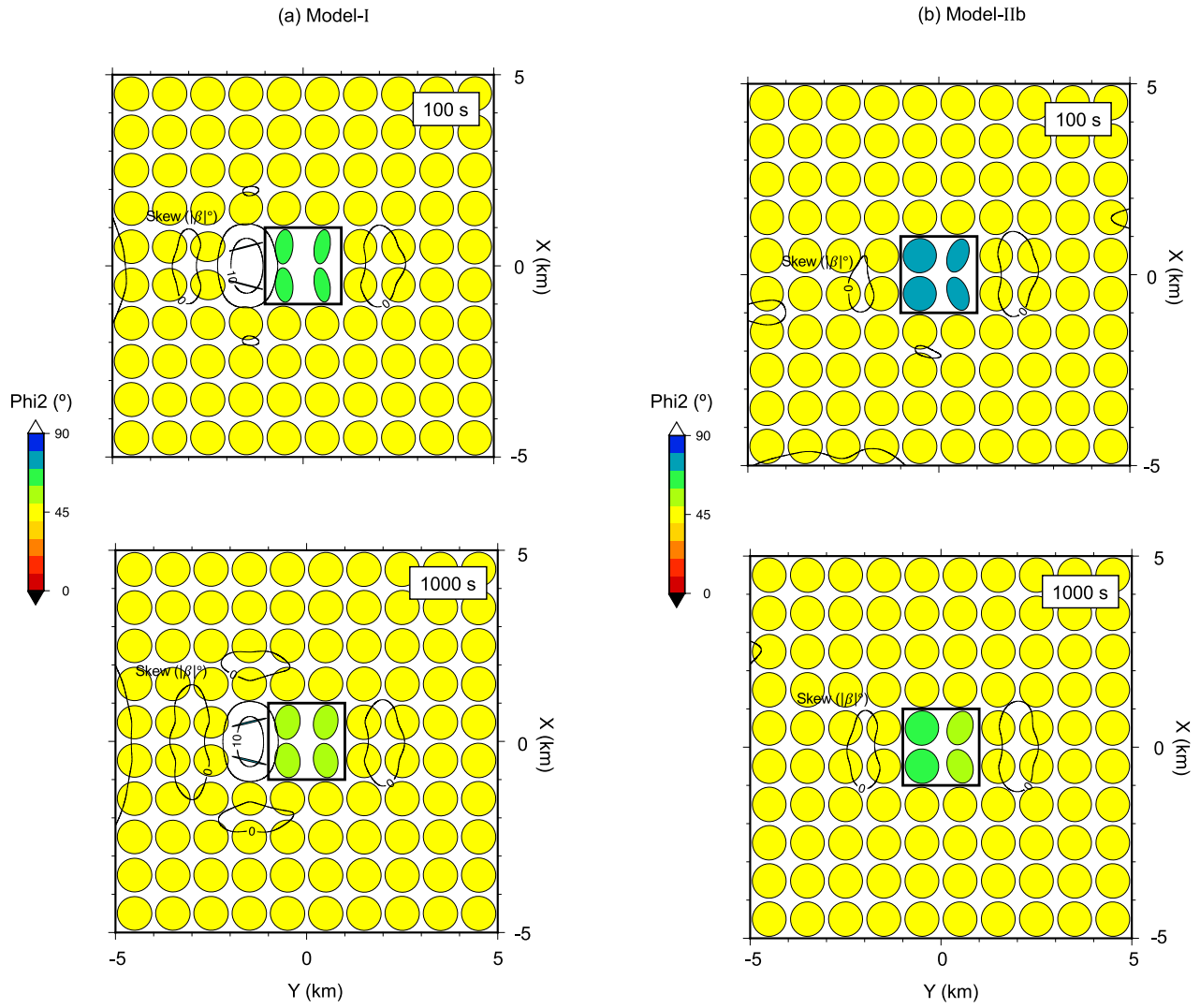


Figure 10. Phase tensor ellipses and the Phi2 at periods of 100 and 1000 s for Model-I (left) and Model-IIb (right). Phase tensor ellipses are normalized by the major axis. The ellipse colour represents the Phi2. The contour represents the absolute value of the skew in the phase tensor.

novel in essence. Meanwhile, unlike the L-shaped (Ichihara & Mogi 2009) and cross-shaped (Raju & Patro 2023) models, in which the conductive bodies appear in contact with each other, the ICC model generates the POQ by a single elongated conductive body embedded in a resistive host rock. We would like to emphasize that the ICC model has broad applicability to real fields precisely because such structures are commonplace and can be found everywhere, providing an intuitive clue to envisage key structures as potential candidates examined in subsequent precise modelling, for example.

Volcanic conduits are one of the natural realizations of the ICC model that we examined above. High-salinity magmatic fluids generally have a low resistivity of less than 1 Ω·m (Sinmyo & Keppler 2017). Therefore, a volcanic conduit containing magmatic fluids may form a strong conductivity contrast to the host rock. Some volcanoes are reported to have oblique conduits because the magma reservoir location revealed by geophysical studies sometimes shows a lateral offset of several kilometres from the active vent of the volcano (Lerner *et al.* 2020). Here, it should be emphasized that the generation of POQ in our model requires a large resistivity contrast; the conductive column should be accompanied by a resistive host rock. Such a high resistivity ranging from hundreds to thousands Ω·m are not particularly rare in actual volcanic fields, and are often interpreted to be dense rocks or basements. Therefore, it is not unreasonable to hypothesize the ICC effect beneath active volcanoes as a candidate mechanism for the POQ. Such ICC-like structures can be actually found in some previous MT studies targeting volcanic regions (e.g. Aizawa *et al.* 2014, 2022; Cordell *et al.* 2018; Matsushima *et al.* 2020; Inoue *et al.* 2022; Matsunaga *et al.* 2022). Among them, Inoue *et al.* (2022) performed 3-D modelling using field data including POQs from the Mt. Meakandake volcano and reported a westward tilting conductive column suggesting a conduit of the volcano. Therein, POQs manifested in the Z_{yx} component at the sites located over the dipping side of the conductive column. Based on a sensitivity test focusing on the POQ, they concluded that the conductive column had a depth extent at least down to 30 km, which is consistent with the present modelling study (Fig. S4, Supporting Information). The Z_{yx} POQ in the periods longer than 100 s is not reproduced by the shortest and the second shortest ICC models, but it is readily generated by those with longer ICCs. Considering the

Downloaded from https://academic.oup.com/gji/article/238/3/1825/7718123 by Hokkaido University user on 26 August 2024

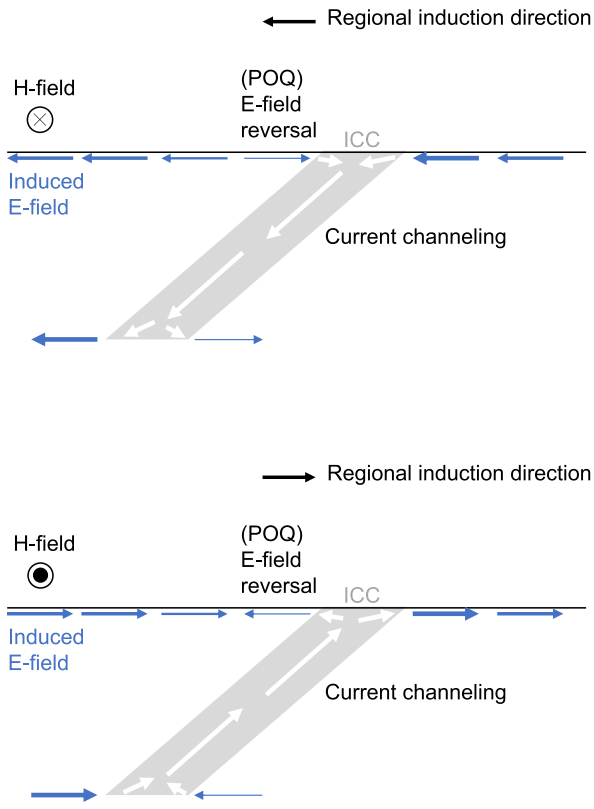


Figure 11. Conceptual diagram summarizing the POQ generation due to an ICC through current channelling. The blue arrows depict the horizontal electric field, with arrow thickness indicating the field's intensity. The white arrows represent the channelled currents in the ICC inferred based on Figs 8 and 9.

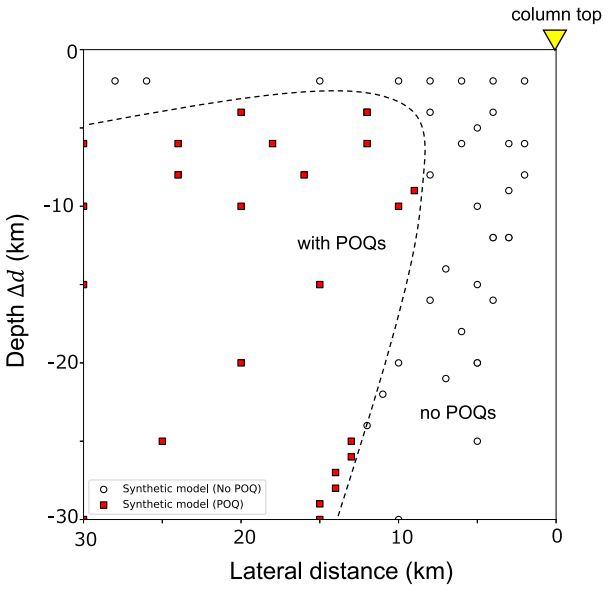


Figure 12. Summary of the synthetic models in this study. The top-right of the figure corresponds to the location of the ICC's top. Symbols correspond to each model with a specific ICC's geometry. The location of each symbol corresponds to the location of the bottom of the ICC for each model. Horizontal axis represents the offset (lateral distance) between the top and bottom of the column. Vertical axis indicates the depth range. The squares indicate the models that are accompanied by anomalous phases (POQ), while the circles do the models without the POQ.

bending point of C1 at 2 km BSL as the top of the ICC, the dip angle is about 60° and therefore, the POQ can appear with this geometry as summarized in Fig. 12. Matsunaga *et al.* (2022) also found an ICC-like anomaly beneath the Kusatsu–Shirane volcano and interpreted it as a magmatic fluid-rich region, where POQs were seen at some MT sites beside the anomaly both in the observation and model response. Considering the synthetic models in our study, the slanted conductive column that they imaged is likely responsible for the generation of the POQ. In addition, Aizawa *et al.* (2014) revealed a conductive column tilting northward beneath the Kirishima volcano based on 3-D inversion modelling using broad-band MT data. Their field data had the POQ in the Z_{xy} component on the north side of the columnar anomaly. The POQ was partially recovered in their inversion. However, their optimal model (Aizawa *et al.* 2014; Fig. 7 [e.g. 512 s]) still maintains a difference of approximately 45° between the model response (phase) and the observed value of the Z_{xy} component at the site on the tilted side of the conductive column. We suspect that a better fit may be achieved when a longer conductive column with a smaller dip angle is introduced, since these parameters can affect the phase response, as mentioned earlier in this study.

4. CONCLUSION

In this study, we examined the MT responses of synthetic models with systematically different ICC geometries, clarifying that the POQ generation conditions are related to the tilt angle and length of the conductive column. The component, in which the POQ emerges, depends on the dip orientation of the ICC. The quasi-static local electric field caused by the strong conductivity contrast between the host rock and the ICC results in a strong distortion. In other words, the localized reverse currents are associated with the current channelling along the conductive column, exhibiting a simple mechanism for the POQ generation. Fluid-rich volcanic conduits are one of the natural realizations of such an ICC; thus, some MT data with the POQ in the previous field studies might be reinterpreted by this ICC effect. Our study implies that the POQ may provide a useful clue for the conduit geometry and the magma plumbing system based on MT surveys particularly in volcanic regions. Of course, we should be aware that a dipping pipe is one possibility along with other previous models for POQs. While our model may not be physically novel in essence, it is possibly one of the simplest 3-D models available in terms of the POQ generation mechanism. Knowledge gained from this study will also help identify key structures and anticipate potential consideration before precise modelling. Conversely, knowing the geological background of the survey area will help in understanding POQs.

ACKNOWLEDGMENTS

This study was supported by JST SPRING (grant no. JPMJSP2119) and the Ministry of Education, Culture, Sports, Science and Technology (MEXT) of Japan (Earthquake and Volcano Observation Research Plan to Contribute to Disaster Mitigation; Research Project No. KYU_01). Helpful discussions with assistant Prof Ryo Tanaka of Hokkaido University improved this content. We gratefully thank anonymous reviewers and the editor for their valuable comments. We used MFB software (Tanaka 2022) as an assistant tool when creating synthetic model. We also used GMT software (Wessel & Smith 1998) and Matplotlib (Hunter 2007) to draw some of the figures.

Downloaded from https://academic.oup.com/gji/article/238/3/1825/7718123 by Hokkaido University user on 26 August 2024

AUTHOR CONTRIBUTIONS

TI and TH contributed to the study conceptualization and discussion. TI carried out the synthetic modelling and visualization. TI drafted the original manuscript. TH carefully checked the modelling results and helped finalizing the manuscript.

SUPPORTING INFORMATION

Supplementary data are available at *GJIRAS* online.

Supplementary_material (8).docx

Please note: Oxford University Press is not responsible for the content or functionality of any supporting materials supplied by the authors. Any queries (other than missing material) should be directed to the corresponding author for the paper.

DATA AVAILABILITY

The response data are available from Tomohiro Inoue on reasonable request.

REFERENCES

Aizawa, K. *et al.* 2014. Three-dimensional resistivity structure and magma plumbing system of the Kirishima Volcanoes as inferred from broadband magnetotelluric data, *J. geophys. Res.,* **119,** 198–215.

Aizawa, K. *et al.* 2022. Magmatic fluid pathways in the upper crust: insights from dense magnetotelluric observations around the Kuju Volcanoes, Japan, *Geophys. J. Int.,* **228,** 755–772.

Arora, B.R. & Adam, A., 1992. Anomalous directional behaviour of induction arrows above elongated conductive structures and its possible causes, *Phys. Earth planet. Int.,* **74,** 3-4, 183–190.

Bologna, M.S., Egbert, G.D., Padilha, A.L., P ádua, M.B. & Vitorello, Í., 2017. 3-D inversion of complex magnetotelluric data from Archean-Proterozoic terrain in northeastern São Francisco Craton, Brazil, *Geophys. J. Int.,* **210,** 1545–1559.

Caldwell, T.G., Bibby, H.M. & Brown, C., 2004. The magnetotelluric phase tensor, *Geophys. J. Int.,* **158,** 457–469.

Cordell, D., Unsworth, M.J. & Diaz, D., 2018. Imaging the Laguna del Maule Volcanic Field, central Chile using magnetotellurics: evidence for crustal melt regions laterally-offset from surface vents and lava flows, *Earth. planet. Sci. Lett.,* **488,** 168–180.

Cordell, D., Unsworth, M.J., Diaz, D., Reyes-Wagner, V., Currie, C.A. & Hicks, S.P., 2019, Fluid and melt pathways in the central Chilean subduction zone near the 2010 Maule earthquake (35–36°, S) as inferred from magnetotelluric data, *Geochem. Geophys. Geosyst.,* **20**(4), 1818–1835.

Egbert, G.D. & Kelbert, A., 2012. Computational recipes for electromagnetic inverse problems, *Geophys. J. Int,* **189,** 251–267.

Heise, W. & Pous, J., 2003. Anomalous phases exceeding 90º in magnetotellurics: anisotropic model studies and a field example, *Geophys. J. Int.,* **155**(1), 308–318.

Hunter, J., 2007. Matplotlib: A 2D graphics environment, *Comput. Sci. Eng.,* **9,** 90–95.

Ichihara, H. *et al.* 2014. A 3-D electrical resistivity model beneath the focal zone of the 2008 Iwate-Miyagi Nairiku earthquake (M 7.2), *Earth Planets Space,* **66,** 50, doi:10.1186/1880-5981-66-50.

Ichihara, H. & Mogi, T., 2009. A realistic 3-D resistivity model explaining anomalous large magnetotelluric phases: the L-shaped conductor model, *Geophys. J. Int.,* **179**(1), 14–17.

Ichihara, H., Mogi, T., Satoh, H. & Yamaya, Y., 2019. Electrical resistivity modeling around the Hidaka collision zone, northern Japan: regional structural background of the 2018 Hokkaido Eastern Iburi earthquake (Mw 6.6), *Earth Planets Space,* **71,** 100, doi:10.1186/s40623-019-1078-7.

Ichihara, H., Mogi, T. & Yamaya, Y., 2013. Three-dimensional resistivity modelling of a seismogenic area in an oblique subduction zone in the western Kurile arc: constraints from anomalous magnetotelluric phases, *Tectonophysics,* **603,** 114–122.

Inoue, T., Hashimoto, T., Tanaka, R. & Yamaya, Y., 2022. A broadband magnetotelluric survey for Mt. Meakandake volcano with special attention to the unrest during 2016-2017, *Earth Planets Space,* **74,** 114, doi:10.1186/s40623-022-01673-8.

Jones, A.G., 1983. The problem of current channelling: a critical review, *Geophys. Surv.,* **6,** 79–122.

Jones, A.G., 1986. Parkinson's pointers' potential perfidy!, *Geophys. J. Int.,* **87**(3), 1215–1224.

Jones, A.G., Kurtz, R.D., Oldenburg, D.W., Boerner, D.E. & Elis, R., 1988. Magnetotelluric observations along the LITHOPROBE southeastern Canadian Cordilleran transect, *Geophys. Res. Lett.,* **15,** 677–680.

Kelbert, A., Mequbel, N., Egbert, G.D. & Tandon, K., 2014. ModEM: a modular system for inversion of electromagnetic geophysical data, *Comput. Geosci.,* **66,** 40–53.

Lerner, A.H., O'Hara, D., Karlstorm, L., Ebmeier, S.K., Anderson, K.R. & Hurwitz, S., 2020. The prevalence and significance of offset magma reservoirs at arc volcanoes, *Geophys. Res. Lett.,***47,** e2020GL087856, doi:10.1029/2020GL087856.

Lezaeta, P. & Haak, V., 2003. Beyond magnetotelluric decomposition: induction, current channeling, and magnetotelluric phases over 90º, *J. geophys. Res.,* **108**(B6), 2305, doi:10.1029/2001JB000990.

Li, X., Bai, D., Chen, Y., Deng, Y., Zhang, S. & Xue, S., 2022. Magnetotelluric signatures of Neoproterozoic subduction, and subsequent lithospheric reactivation and thinning beneath central South China, *Geophys. J. Int.,* **833,** 229365, doi: 10.1016/j.tecto.2022.229365.

Livelybrooks, D., Mareschal, M., Blais, E. & Smith, J.T., 1996. Magnetotelluric delineation of the Trillabelle massive sulfide body in Sudbury, Ontario, *Geophysics,* **61,** 971–986.

Matsunaga, Y., Kanda, W., Koyama, T., Takakura, S. & Nishizawa, T., 2022. Large-scale magmatic-hydrothermal system of Kusatsu-Shirane Volcano, Japan, revealed by broadband magnetotellurics, *J. Volc. Geotherm. Res.,* **429,** 107600, doi:10.1016/j.jvolgeores.2022.107600.

Matsushima, N., Utsugi, M., Takakura, S., Yamasaki, T., Hata, M., Hashimoto, T. & Uyeshima, M., 2020. Magmatic-hydrothermal system of Aso Volcano, Japan, inferred from electrical resistivity structures, *Earth Planet Space.,* **72,** 57, doi:10.1186/s40623-020-01180-8.

Parkinson, W.D., 1959. Directions of rapid geomagnetic fluctuations, *Geophys. J. Int.,* **2**(1), 1–14.

Pavan Kumar, G. & Manglik, A., 2012. Electrical anisotropy in the Main Central Thrust Zone of the Sikkim Himalaya: inference from anomalous MT phase, *J. Asian Earth Sci.,* **57,** 120–127.

Pek, J. & Verner, T., 1997. Finite-difference modelling of magnetotelluric fields in two-dimensional anisotropic media, *Geophys. J. Int.,* **128,** 505–521.

Piña-Varas, P.P. & Dentith, M., 2018. Magnetotelluric data from the Southeastern Capricorn Orogen, Western Australia: an example of widespread out-of-quadrant phase responses associated with strong 3-D resistivity contrasts, *Geophys. J. Int.,* **212,** 1022–1032.

Pous, J., Heise, W., Schnegg, P.A., Munoz, G., Marti., J. & Soriano, C., 2002. Magnetotelluric study of the Las Canadas caldera (Tenerife, Canary Islands): structural and hydrogeological implications, *Earth. planet. Sci. lett.,* **204,** 249–263.

Raju, K. & Patro, P.K., 2023. Modelling of subsurface geological structure related to anomalous magnetotelluric phase data exceeding 90º in Central India, *Geophys. J. Int.,* **235,** 1671–1680.

Raju, K., Patro, P.K., Borah, U.K., Srivasta, S. & Reddy, K.C., 2022, Evolution of eastern segment of the Central India Tectonic Zone: an insight from a magnetotelluric study, *Geophys. J. Int.,* **230,** 272–287.

Rippe, D., Unsworth, M.J. & Currie., C.A., 2013. Magnetotelluric constraints on the fluid content in the upper mantle beneath the southern Canadian Cordillera: implications for rheology, *J. geophys Res: Solid Earth,* **118,** 5601–5624.

Selway, K., Thiel, S. & Key, K., 2012. A simple 2-D explanation for negative phases in TE magnetotelluric data, *Geophys. J. Int.,* **188**(3), 945–958.

Downloaded from https://academic.oup.com/gji/article/238/3/1825/7718123 by Hokkaido University user on 26 August 2024

Sinmyo, R. & Keppler, H., 2017. Electrical conductivity of NaCl-bearing aqueous fluids to 600 °C and 1 GPa, *Contrib. Mineral. Petrol.,* **172**(1), Article No. 4, doi: 10.1007/s00410-016-1323-z.

Siripunvaraporn, W. & Egbert, G., 2009. WSINV3DMT: vertical magnetic field transfer function inversion and parallel implementation, *Phys. Earth. Planet Inter.,* **173,** 317–329.

Tanaka, R., 2022. Simple graphical pre- and post-processor for 3-D magnetotelluric inversion, *J. Disaster Res.,* **17,** 639–643.

Thiel, S., Heinson, G., Gray, D.R. & Gregory, R.T., 2009, Ophiolite emplacement in NE Oman: constraints from magnetotelluric sounding, *Geophys. J. Int.,* **176,** 753–766.

Usui, Y., 2015. 3-D inversion of magnetotelluric data using unstructured tetrahedral elements: applicability to data affected by topography, *Geophys. J. Int.,* **202,** 828–849.

Uyeshima, M., Utada, H. & Nishida, Y., 2001. Network-magnetotelluric method and its first results in central and eastern Hokkaido, NE Japan, *Geophys. J. Int,* **146,** 1–19.

Weckmann, U., Ritter, O. & Haak, V., 2003. A magnetotelluric study of the Damara Belt in Namibia: 2. MT phases over 90° reveal the internal structure of the Waterberg Fault/Omaru Lineament, *Phys. Earth planet. Inter.,* **138**(2), 91–112.

Wessel, P. & Smith, W.H.F., 1998. New, improved version of the Generic Mapping Tools released, *EOS, Trans. Am. geophys. Un.,* **79,** 579, doi:10.1029/98EO00426.

Zhang, S., Yu, N., Wang, E., Li, D., Li, R. & Liu, Y., 2021. The seismogenic structure and dynamic environment of Wulong Ms 5.0 earthquake revealed by magnetotelluric imaging, *Tectonophysics,* **811,** 228867, doi:10.1016/j.tecto.2021.228867.

Downloaded from https://academic.oup.com/gji/article/238/3/1825/7718123 by Hokkaido University user on 26 August 2024

© The Author(s) 2024. Published by Oxford University Press on behalf of The Royal Astronomical Society. This is an Open Access article distributed under the terms of the Creative Commons Attribution License (https://creativecommons.org/licenses/by/4.0/), which permits unrestricted reuse, distribution, and reproduction in any medium, provided the original work is properly cited.